Commun. Comput. Phys.
doi: 10.4208/cicp.scpde14.43s

Vol. **19**, No. 5, pp. 1111-1140
May 2016

Entropy Stable Scheme on Two-Dimensional Unstructured Grids for Euler Equations

Deep Ray[1], Praveen Chandrashekar[1], Ulrik S. Fjordholm[2] and Siddhartha Mishra[3,*]

[1] *Tata Institute of Fundamental Research, Centre for Applicable Mathematics, Bengaluru, India.*
[2] *Department of Mathematical Sciences, NTNU, Trondheim 7491, Norway.*
[3] *Seminar for Applied Mathematics, ETH Zurich and Center of Mathematics for Applications, University of Oslo, Norway.*

Received 13 April 2015; Accepted 29 December 2015

Abstract. We propose an entropy stable high-resolution finite volume scheme to approximate systems of two-dimensional symmetrizable conservation laws on unstructured grids. In particular we consider Euler equations governing compressible flows. The scheme is constructed using a combination of entropy conservative fluxes and entropy-stable numerical dissipation operators. High resolution is achieved based on a linear reconstruction procedure satisfying a suitable sign property that helps to maintain entropy stability. The proposed scheme is demonstrated to robustly approximate complex flow features by a series of benchmark numerical experiments.

AMS subject classifications: 65M08, 35L65, 35Q31

Key words: Entropy stability, Euler equations, unstructured grids, sign property, higher-order accuracy.

1 Introduction

Systems of conservation laws are encountered in numerous fields of science and engineering. Examples include the shallow water equations of oceanography, the Euler equations of aerodynamics and the MHD equations of plasma physics. In two space dimensions, a generic system of conservation laws is given by

$$\begin{aligned}&\partial_t \mathbf{U}+\partial_x \mathbf{f}_1(\mathbf{U})+\partial_y \mathbf{f}_2(\mathbf{U})=0 \qquad \forall\, \mathbf{x}=(x,y)\in\mathbb{R}^2,\ t\in\mathbb{R}^+\\ &\mathbf{U}(\mathbf{x},0)=\mathbf{U}_0(\mathbf{x}) \qquad \forall\, \mathbf{x}\in\mathbb{R}^2.\end{aligned} \tag{1.1}$$

*Corresponding author. *Email addresses:* `deep@tifrbng.res.in` (D. Ray), `praveen@tifrbng.res.in` (P. Chandrashekar), `ulrik.fjordholm@math.ntnu.no` (U. S. Fjordholm), `siddhartha.mishra@sam.math.ethz.ch` (S. Mishra)

In the above equations, the vector of conserved variables is denoted by $\mathbf{U}: \mathbb{R}^2 \times \mathbb{R}^+ \to \mathbb{R}^n$, $\mathbf{f}_1, \mathbf{f}_2$ are the Cartesian components of the flux vector and $\mathbf{U}_0$ is the prescribed initial condition. In particular, for the two-dimensional compressible Euler equations, we have

$$\mathbf{U} = \begin{pmatrix} \rho \\ \rho u \\ \rho v \\ E \end{pmatrix}, \qquad \mathbf{f}_1(\mathbf{U}) = \begin{pmatrix} \rho u \\ \rho u^2 + p \\ \rho u v \\ u(E+p) \end{pmatrix}, \qquad \mathbf{f}_2(\mathbf{U}) = \begin{pmatrix} \rho v \\ \rho u v \\ \rho v^2 + p \\ v(E+p) \end{pmatrix}, \tag{1.2}$$

where ρ, $\mathbf{u} = (u,v)^\top$ and p denote the fluid density, velocity and pressure, respectively. The quantity E is the total energy per unit volume

$$E = \rho\left(\frac{1}{2}(u^2+v^2) + e\right), \tag{1.3}$$

where e is the specific internal energy given by a caloric equation of state, $e = e(\rho, p)$. In this work, we take the equation of state for ideal gas as given by

$$e = \frac{p}{(\gamma-1)\rho} \tag{1.4}$$

with $\gamma = c_p/c_v$ denoting the ratio of specific heats.

It is well known that solutions to systems of conservation laws can develop discontinuities, such as shock waves and contact discontinuities, in finite time even when the initial data is smooth [11]. Hence, the solutions of systems of conservation laws are interpreted in a weak (distributional) sense. However, these weak solutions are not necessarily unique, and must be supplemented with additional conditions, known as the *entropy conditions*, in order to single out a physically relevant solution. Assume that for the system (1.1), there exists a convex function $\eta: \mathbb{R}^n \to \mathbb{R}$ and functions $q_i: \mathbb{R}^n \to \mathbb{R}$, $i = 1,2$ such that

$$q_i'(\mathbf{U}) = \eta'(\mathbf{U})^\top \mathbf{f}_i'(\mathbf{U}), \qquad i = 1,2. \tag{1.5}$$

The function η is known as an *entropy function*, while q_1, q_2 are the *entropy flux functions*. Additionally, $\mathbf{V} = \eta'(\mathbf{U})$ is called the (vector of) *entropy variables*. Multiplying (1.1) by $\mathbf{V}^\top$ results in the following additional conservation law for smooth solutions:

$$\partial_t \eta(\mathbf{U}) + \partial_x q_1(\mathbf{U}) + \partial_y q_2(\mathbf{U}) = 0. \tag{1.6}$$

The entropy condition states that weak solutions should satisfy the entropy inequality

$$\partial_t \eta(\mathbf{U}) + \partial_x q_1(\mathbf{U}) + \partial_y q_2(\mathbf{U}) \leqslant 0, \tag{1.7}$$

which is understood in the sense of distributions.

The convexity of $\eta(\mathbf{U})$ ensures the existence of a one-to-one mapping between $\mathbf{U}$ and $\mathbf{V}$, thus allowing the change of variables $\mathbf{U} = \mathbf{U}(\mathbf{V})$. The hyperbolic system (1.1) is *symmetrized* when written in terms of the entropy variables. In other words, for the transformed system

$$\partial_{\mathbf{V}} \mathbf{U} \partial_t \mathbf{V} + \partial_{\mathbf{V}} \mathbf{f}_1 \partial_x \mathbf{V} + \partial_{\mathbf{V}} \mathbf{f}_2 \partial_y \mathbf{V} = 0$$

the Jacobian $\partial_{\mathbf{V}}\mathbf{U}$ is symmetric positive definite, while $\partial_{\mathbf{V}}\mathbf{f}_1, \partial_{\mathbf{V}}\mathbf{f}_2$ are symmetric. In this direction, we have the important results due to Godunov [20] and Mock [34], which state that the hyperbolic system (1.1) is symmetrizable if and only if it is equipped with an entropy function $\eta(\mathbf{U})$ and corresponding entropy fluxes $q_1(\mathbf{U}), q_2(\mathbf{U})$.

Although no global existence and uniqueness results for entropy solutions of these systems are currently available, the entropy conditions do play an important role in providing global stability estimates. Formally integrating (1.7) in space and ignoring the boundary terms by assuming periodic or no-inflow boundary conditions, we get

$$\frac{\mathrm{d}}{\mathrm{d}t}\int_{\mathbb{R}^2}\eta(\mathbf{U})\mathrm{d}\mathbf{x} \leqslant 0 \quad \Longrightarrow \quad \int_{\mathbb{R}^2}\eta(\mathbf{U}(\mathbf{x},t))\mathrm{d}\mathbf{x} \leqslant \int_{\mathbb{R}^2}\eta(\mathbf{U}_0(\mathbf{x}))\mathrm{d}\mathbf{x}, \qquad \forall\, t>0. \tag{1.8}$$

As η is convex, the above entropy bound gives rise to an a priori estimate on the solution of (1.1) in suitable L^p spaces [11].

Numerical methods for hyperbolic systems have undergone extensive development over the past few decades. Finite volume methods, in which the computational domain is divided into control volumes and a discrete version of the conservation law imposed on each control volume, are very popular. In particular, (approximate) Riemann solver based numerical flux functions, non-oscillatory reconstructions of the TVD, ENO, WENO type and strong stability preserving Runge-Kutta methods constitute an attractive and widely used package for the robust approximation of systems of conservation laws. An alternative is the use of Runge-Kutta Discontinuous Galerkin (DG) finite element methods [9] together with limiters to obtain non-oscillatory approximation.

Although many rigorous convergence results for these methods (at least for their first and second-order versions) are known for *scalar conservation laws*, even in several space dimensions (see [29, 30] and references therein), very few rigorous results are available for schemes approximating systems of conservation laws, particularly in several space dimensions. Since obtaining rigorous convergence results of numerical approximation to entropy solutions seems out of reach currently (see [18] for a discussion on this issue) the design of *entropy stable schemes* – numerical schemes that satisfy a discrete form of the entropy inequality (1.7) – is a reasonable goal. Note that entropy stable schemes automatically satisfy an L^p estimate and provide the only global stability estimates currently available for numerical methods for multi-dimensional conservation laws.

The construction of entropy stable schemes for systems of conservation laws was pioneered by Tadmor in [44]. The construction is based on two ingredients – *(i)* construction of an entropy conservative flux satisfying a discrete entropy equality, and *(ii)* addition of suitable dissipation operators to satisfy a discrete entropy inequality. First-order entropy stable schemes, in which the solution is assumed to be piecewise constant in the cells, have been tested by Fjordholm et al. [15] for the shallow-water equations and by Roe and Ismail [24] for the Euler equations on Cartesian meshes, and found to be efficient. High-order accurate schemes are constructed by reconstructing the solution in each cell by a polynomial. Arbitrarily high-order entropy conservative fluxes for Cartesian grids were developed in [31]. However, the design of arbitrary-high-order entropy stable schemes was only carried out recently by Fjordholm et al. in [16]. These so-called *TeCNO schemes* judiciously combine high-order entropy conservative fluxes with arbitrarily high-order numerical diffusion operators, based on piecewise polynomial reconstruction. The reconstructions have to satisfy a *sign property* at each interface to ensure entropy stability. This means that the jump in the reconstructed values at every cell face must have the same sign as the jump in the corresponding cell values. It was shown in [17] that the standard ENO reconstruction procedure does satisfy the sign property. The resulting TeCNO schemes are only available for Cartesian (structured) grids in several space dimensions. However, many applications of interest, particularly in engineering, involve domains with complex geometry [13,26] which can be more easily discretized using *unstructured grids*.

The construction of high resolution, entropy stables schemes on unstructured grids is not as mature, which is the main aim of this paper. In [32], a first-order finite volume scheme was constructed in the framework of cell-centered schemes, where the solution is stored at the center of the cells. It does not seem to be possible to extend this approach to high resolution while at the same time maintaining the sign property and the accuracy of the scheme. In this work, we use a vertex-centered finite volume scheme where the solution is stored at the vertices of the mesh and a dual cell is constructed around each vertex on which the conservation law is satisfied [1,2,33,35,42,49]. The high resolution scheme is constructed by using a reconstruction process to obtain the solution values at the faces of the cells. In the literature, there are several approaches to perform this reconstruction [5,6,10,14,28,35,39,40,46–48]. We use a simple approach for reconstruction, (see e.g., chapter IV - section 5.1 of [19]), but this process is combined with the structure of the dissipation operator so that the sign property can be satisfied. We hence construct a semi-discrete, high resolution scheme which is entropy stable on general triangulations. The fully discrete scheme is obtained by using a Runge-Kutta scheme for time integration.

The rest of the paper is organized as follows. In Section 2 we describe the discretization of the domain and introduce the general semi-discrete scheme for system of conservation laws. Section 3 introduces the machinery for construction of entropy conservative and entropy stable schemes. Construction of higher-order entropy stable schemes by the limited reconstruction of scaled entropy variables is also discussed. Several two-dimensional numerical results are presented in Section 4 to demonstrate the robustness of the proposed schemes. Concluding remarks are made in Section 5.

2 Mesh and finite volume scheme

The domain $\Omega \subset \mathbb{R}^2$ is discretized using disjoint triangles T with nodes denoted by i,j,k, etc., which forms the *primary mesh*. For each edge of a triangle, we define the outward normal vectors with magnitude equal to the length of the corresponding edge. We use the notation $\mathbf{n}_i^T$ to describe the outward normal to the edge of T which is opposite to the vertex i. Furthermore, for each boundary edge e we denote the triangle adjacent to it by

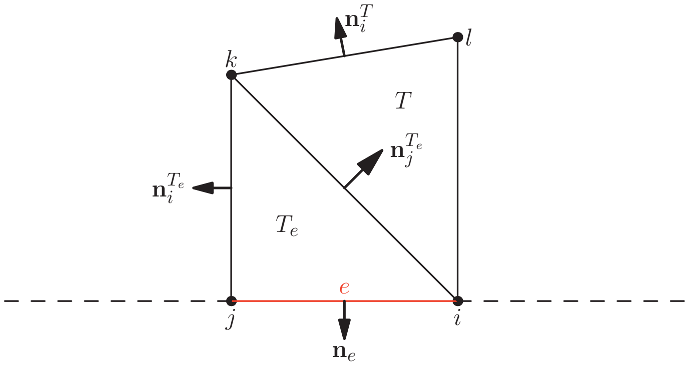

Figure 1: Triangle T and T_e with outward normals.

T_e and the outward normal to the edge e as $\mathbf{n}_e$. These are depicted in Fig. 1.

Around each vertex i, the dual cell is constructed by joining the centroids of each adjoining triangle to the mid-points of its edges. This is known as the *median dual cell* [2, 42,49]. The *Voronoi dual cells* can also be generated in a similar manner by joining the mid-point of the triangle edges to the circumcenters instead of the centroids [1,33]. Examples of primary meshes and corresponding dual meshes are depicted in Fig. 2. We adopt the *vertex-centered* approach for the finite volume schemes discussed below, where the dual cells are chosen as the control volumes and the solution (cell average) is stored at the nodes.

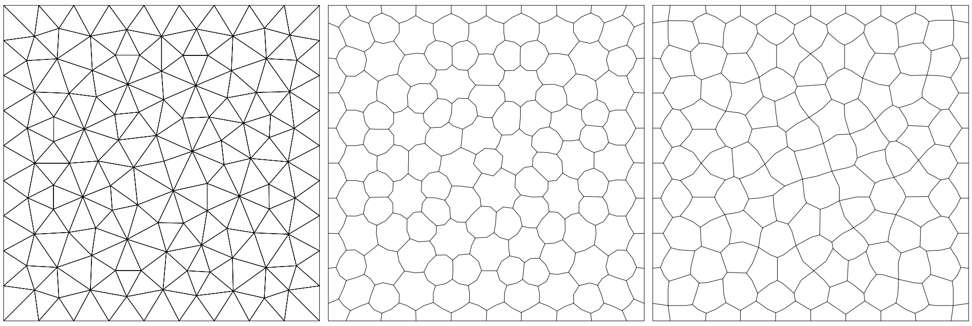

(a) (b) (c)

Figure 2: Mesh (a) primary; (b) median dual; (c) Voronoi dual.

Consider the dual cell C_i around vertex i as shown in Fig. 3. If j is a vertex connected to vertex i, then define

$$\mathbf{n}_{ij} = \int_{\partial C_i \cap \partial C_j} \tilde{\mathbf{n}} ds = \mathbf{n}_{ij}^{(1)} + \mathbf{n}_{ij}^{(2)},$$

where $\tilde{\mathbf{n}}$ is the unit normal vector to the faces of dual cell C_i common with the dual cell C_j. The quantity $\mathbf{n}_{ij}$ has units of length. The notation $j \in i$ will denote the set of vertices

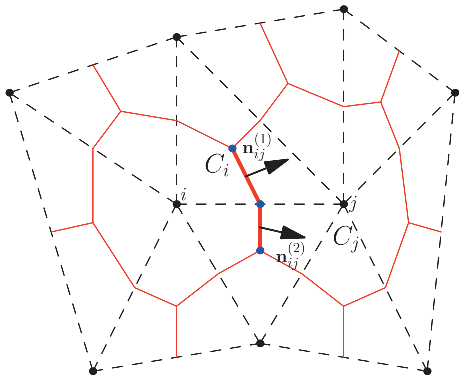

Figure 3: Dual cell interface and normal.

j neighbouring the vertex i, i.e., which are connected to vertex i through an edge. The semi-discrete finite volume scheme corresponding to (1.1) is given by

$$\frac{\mathrm{d}\mathbf{U}_i}{\mathrm{d}t}+\frac{1}{|C_i|}\sum_{j\in i}\mathbf{F}_{ij}=0, \tag{2.1}$$

where $\mathbf{U}_i$ is the cell average over the dual cell C_i and $\mathbf{F}_{ij}=\mathbf{F}(\mathbf{U}_i,\mathbf{U}_j,\mathbf{n}_{ij})$ is the numerical flux function satisfying the following properties.

1. **Consistency:**
$$\mathbf{F}(\mathbf{U},\mathbf{U},\mathbf{n})=\mathbf{f}(\mathbf{U},\mathbf{n}), \qquad \forall\ \mathbf{U},\mathbf{n}.$$

2. **Conservation:**
$$\mathbf{F}(\mathbf{U}_1,\mathbf{U}_2,\mathbf{n})=-\mathbf{F}(\mathbf{U}_2,\mathbf{U}_1,-\mathbf{n}), \qquad \forall\ \mathbf{U}_1,\mathbf{U}_2,\mathbf{n}.$$

Here, we have denoted $\mathbf{f}(\mathbf{U},\mathbf{n}):=\mathbf{f}_1(\mathbf{U})n_1+\mathbf{f}_2(\mathbf{U})n_2$.

3 Entropy conservative and entropy stable schemes

As mentioned in the introduction, we aim to construct an entropy stable scheme to approximate (1.1). Following Tadmor [43] and the recent paper [32], the first step is the design of an entropy conservative scheme, as outlined below.

3.1 Entropy conservative scheme

Definition 3.1. The numerical scheme (2.1) is said to be *entropy conservative* if it satisfies the discrete entropy relation

$$\frac{\mathrm{d}\eta(\mathbf{U}_i)}{\mathrm{d}t}+\frac{1}{|C_i|}\sum_{j\in i}q_{ij}^*=0, \tag{3.1}$$

where q_{ij}^* is a consistent numerical entropy flux.

We introduce the following notation

$$\Delta(\cdot)_{ij} = (\cdot)_j - (\cdot)_i, \qquad \overline{(\cdot)}_{ij} = \frac{(\cdot)_i + (\cdot)_j}{2}.$$

Moreover, we introduce the *entropy potential*

$$\psi(\mathbf{U},\mathbf{n}) := \mathbf{V}(\mathbf{U})^\top \mathbf{F}(\mathbf{U},\mathbf{n}) - q(\mathbf{U},\mathbf{n}),$$

where $q(\mathbf{U},\mathbf{n}) := q_1(\mathbf{U})n_1 + q_2(\mathbf{U})n_2$. The next theorem gives a sufficient condition on the numerical flux which makes the scheme entropy conservative, which is a variant of the result in [32] for cell-centered schemes.

Theorem 3.1. *The numerical scheme* (2.1) *with the flux* $\mathbf{F}^*$ *is entropy conservative if*

$$\Delta\mathbf{V}_{ij}^\top \mathbf{F}_{ij}^* = \psi(\mathbf{U}_j,\mathbf{n}_{ij}) - \psi(\mathbf{U}_i,\mathbf{n}_{ij}). \tag{3.2}$$

Specifically, it satisfies (3.1) *with numerical entropy flux given by*

$$q_{ij}^* = q^*(\mathbf{U}_i,\mathbf{U}_j,\mathbf{n}_{ij}) = \overline{\mathbf{V}}_{ij}^\top \mathbf{F}_{ij}^* - \frac{1}{2}\left(\psi(\mathbf{U}_j,\mathbf{n}_{ij}) + \psi(\mathbf{U}_i,\mathbf{n}_{ij})\right).$$

Proof. Multiplying (2.1) by the entropy variables $\mathbf{V}_i$, we get

$$\begin{aligned}
\frac{\mathrm{d}}{\mathrm{d}t}\eta(\mathbf{U}_i) &= -\frac{1}{|C_i|}\sum_{j\in i}\mathbf{V}_i^\top \mathbf{F}_{ij}^* \\
&= -\frac{1}{|C_i|}\sum_{j\in i}\left(\overline{\mathbf{V}}_{ij} - \frac{1}{2}\Delta\mathbf{V}_{ij}\right)^\top \mathbf{F}_{ij}^* \\
&= -\frac{1}{|C_i|}\sum_{j\in i}\left(\overline{\mathbf{V}}_{ij}^\top \mathbf{F}_{ij}^* - \frac{1}{2}\left(\psi(\mathbf{U}_j,\mathbf{n}_{ij}) - \psi(\mathbf{U}_i,\mathbf{n}_{ij})\right)\right) \\
&= -\frac{1}{|C_i|}\sum_{j\in i}\left(\overline{\mathbf{V}}_{ij}^\top \mathbf{F}_{ij}^* - \frac{1}{2}\left(\psi(\mathbf{U}_j,\mathbf{n}_{ij}) + \psi(\mathbf{U}_i,\mathbf{n}_{ij})\right)\right) - \frac{1}{|C_i|}\sum_{j\in i}\psi(\mathbf{U}_i,\mathbf{n}_{ij}) \\
&= -\frac{1}{|C_i|}\sum_{j\in i} q_{ij}^*,
\end{aligned}$$

where we have used the fact that $\sum_{j\in i}\psi(\mathbf{U}_i,\mathbf{n}_{ij}) = 0$ since $\sum_{j\in i}\mathbf{n}_{ij} = 0$. □

Harten [22] has shown that the Euler equations are equipped with a family of entropy-entropy flux functions of the form

$$\eta(\mathbf{U}) = -\frac{\rho h(s)}{\gamma-1}, \qquad q_1(\mathbf{U}) = -\frac{\rho u h(s)}{\gamma-1}, \qquad q_2(\mathbf{U}) = -\frac{\rho v h(s)}{\gamma-1}$$

with an additional constraint $h''/h' < \gamma^{-1}$ to enforce convexity of η. Here $s = \ln(p) - \gamma\ln(\rho)$ is the non-dimensional specific entropy. Hughes et al. [23] have shown that this form of entropy-entropy flux functions can be extended to the Navier-Stokes equations, where the symmetrization of the heat conduction term puts the restriction that $h(s)$ can be at most affine. A convenient choice which we adhere to for the rest of this paper is

$$\eta(\mathbf{U}) = -\frac{\rho s}{\gamma-1}, \qquad q_1(\mathbf{U}) = -\frac{\rho u s}{\gamma-1}, \qquad q_2(\mathbf{U}) = -\frac{\rho v s}{\gamma-1}. \tag{3.3}$$

The corresponding entropy variables $\mathbf{V}$ are given by

$$\mathbf{V} = \left(\tfrac{\gamma-s}{\gamma-1} - \beta|\mathbf{u}|^2, \quad 2\beta\mathbf{u}, \quad -2\beta\right)^\top, \tag{3.4}$$

where $\beta = \rho/(2p)$. Next, we briefly describe two important examples of entropy conservative fluxes which have been designed for the Euler equations.

Example 3.1. Roe and Ismail [24] have constructed a numerical flux for the Euler equations satisfying (3.2). They introduce the parameter vector

$$\mathbf{Z} = \sqrt{\frac{\rho}{p}}\left(1, \quad u, \quad v, \quad p\right)^\top$$

and write the entropy conservative flux in terms of $\mathbf{Z}$ as follows.

$$\mathbf{F}^*_{ij} = \begin{pmatrix} F^{*,\rho} \\ F^{*,m1} \\ F^{*,m2} \\ F^{*,e} \end{pmatrix} = \begin{pmatrix} \overline{Z_n}\widehat{Z_4} \\ \frac{\overline{Z_4}}{\overline{Z_1}}n_1 + \frac{\overline{Z_2}}{\overline{Z_1}}F^{*,\rho} \\ \frac{\overline{Z_4}}{\overline{Z_1}}n_2 + \frac{\overline{Z_3}}{\overline{Z_1}}F^{*,\rho} \\ F^{*,e} \end{pmatrix}, \qquad F^{*,e} = \frac{1}{2\overline{Z_1}}\left[\frac{(\gamma+1)}{(\gamma-1)}\frac{F^{*,\rho}}{\widehat{Z_1}} + \overline{Z_2}F^{*,m1} + \overline{Z_3}F^{*,m2}\right],$$

where

$$\overline{Z_n} = \overline{Z_2}n_1 + \overline{Z_3}n_2$$

and $\widehat{\phi}_{ij} = \frac{\phi_j - \phi_i}{\ln(\phi_j) - \ln(\phi_i)}$ is the logarithmic average which is well defined for strictly positive quantities ϕ.

Example 3.2. An entropy conservative flux for the Euler equations, which also preserves kinetic energy was introduced in [8]. This is given by

$$\mathbf{F}^* = \begin{pmatrix} F^{*,\rho} \\ F^{*,m1} \\ F^{*,m2} \\ F^{*,e} \end{pmatrix} = \begin{pmatrix} \widehat{\rho}\overline{u}_n \\ \tilde{p}n_1 + \overline{u}F^{*,\rho} \\ \tilde{p}n_2 + \overline{v}F^{*,\rho} \\ F^{*,e} \end{pmatrix}, \qquad F^{*,e} = \left[\frac{1}{2(\gamma-1)\widehat{\beta}} - \frac{1}{2}\overline{|\mathbf{u}|^2}\right]F^{*,\rho} + \overline{\mathbf{u}}\cdot\mathbf{F}^{*,m}, \tag{3.5}$$

where

$$\overline{u}_n = \overline{u}n_1 + \overline{v}n_2, \qquad \tilde{p} = \frac{\overline{\rho}}{2\overline{\beta}}$$

and $\widehat{\rho}$, $\widehat{\beta}$ are the logarithmic averages of the respective quantities. The crucial property for kinetic energy preservation as given by Jameson [27], is that the momentum flux should be of the form $\mathbf{F}^m = p\mathbf{n} + \overline{\mathbf{u}}F^\rho$ for any consistent approximations for the pressure p and the mass flux F^ρ.

Remark 3.1. Entropy conservative fluxes described above can be shown to be second-order accurate on cartesian meshes, in terms of the local truncation [44]. The same proof can be used to show the validity of this result for the vertex-centered setup on unstructured meshes.

3.2 First-order entropy stable scheme

The entropy of hyperbolic conservation laws is conserved only if the solution is smooth. However, entropy is dissipated near discontinuities like shocks, in accordance to the entropy condition (1.7). It is well known [44] that an entropy conservative scheme, although suitable for smooth solutions, can be very oscillatory at shocks. Hence, we need to introduce additional dissipation terms to construct entropy stable schemes.

Definition 3.2. The numerical scheme (2.1) is said to be *entropy stable* if it satisfies the discrete entropy relation

$$\frac{\mathrm{d}\eta(\mathbf{U}_i)}{\mathrm{d}t}+\frac{1}{|C_i|}\sum_{j\in i}q_{ij}\leqslant 0, \tag{3.6}$$

where q_{ij} is a consistent numerical entropy flux.

To dissipate entropy we follow [16, 44] and add entropy variable-based numerical dissipation to the entropy conservative numerical flux $\mathbf{F}^*_{ij}$ in the form

$$\mathbf{F}_{ij}=\mathbf{F}^*_{ij}-\frac{1}{2}\mathbf{D}_{ij}\Delta\mathbf{V}_{ij} \tag{3.7}$$

for a symmetric positive semi-definite matrix $\mathbf{D}_{ij}$, i.e., $\mathbf{D}_{ij}=\mathbf{D}_{ij}^\top\geqslant 0$. The diffusion matrix must also satisfy $\mathbf{D}_{ij}=\mathbf{D}_{ji}$ to ensure that the numerical flux is conservative. The following lemma has been proved for the cell-centered setup in [32], which we adapt for vertex-centered schemes.

Lemma 3.1. *The semi-discrete numerical scheme* (2.1) *with numerical flux given by* (3.7) *is entropy stable; specifically, it satisfies the discrete entropy inequality* (3.6) *with numerical entropy flux given by*

$$q_{ij}=q^*_{ij}-\frac{1}{2}\overline{\mathbf{V}}_{ij}^\top\mathbf{D}_{ij}\Delta\mathbf{V}_{ij}.$$

Proof. Multiplying (2.1) by $\mathbf{V}_i$ and following the algebraic manipulations similar to those in Theorem 3.1, we get

$$\begin{aligned}\frac{\mathrm{d}}{\mathrm{d}t}\eta(\mathbf{U}_i) &= -\frac{1}{|C_i|}\sum_{j\in i}\mathbf{V}_i^\top \mathbf{F}_{ij} \\ &= -\frac{1}{|C_i|}\sum_{j\in i}\left[q_{ij}^* - \frac{1}{2}\left(\overline{\mathbf{V}}_{ij} - \frac{1}{2}\Delta\mathbf{V}_{ij}\right)^\top \mathbf{D}_{ij}\Delta\mathbf{V}_{ij}\right] \\ &= -\frac{1}{|C_i|}\sum_{j\in i} q_{ij} - \frac{1}{4|C_i|}\sum_{j\in i}\Delta\mathbf{V}_{ij}^\top \mathbf{D}_{ij}\Delta\mathbf{V}_{ij} \\ &\leqslant -\frac{1}{|C_i|}\sum_{j\in i} q_{ij}\end{aligned}$$

since $\Delta\mathbf{V}_{ij}^\top \mathbf{D}_{ij}\Delta\mathbf{V}_{ij} \geqslant 0$. Moreover it is easy to see that q_{ij} as defined in the theorem is a consistent numerical entropy flux. □

3.3 Dissipation operator

To construct the dissipation matrix $\mathbf{D}_{ij}$ we take inspiration from Roe's approximate Riemann solver [38], which is based on the linearization of the nonlinear conservation law about some average state. The numerical flux of the Roe scheme has the form

$$\mathbf{F}_{ij} = \frac{1}{2}\left(\mathbf{f}(\mathbf{U}_i,\mathbf{n}_{ij}) + \mathbf{f}(\mathbf{U}_j,\mathbf{n}_{ij})\right) - \frac{1}{2}\mathbf{R}_{ij}\mathbf{\Lambda}_{ij}\mathbf{R}_{ij}^{-1}\Delta\mathbf{U}_{ij}, \tag{3.8}$$

where $\mathbf{R} = \mathbf{R}(\mathbf{U},\mathbf{n})$ is the matrix of eigenvectors of the flux Jacobian $\partial_{\mathbf{U}}\mathbf{f}(\mathbf{U},\mathbf{n})$ and $\mathbf{\Lambda} = \mathbf{\Lambda}(\mathbf{U},\mathbf{n})$ is the non-negative diagonal matrix

$$\mathbf{\Lambda} = \mathrm{diag}\Big(|\lambda_1|,\cdots,|\lambda_n|\Big) \tag{3.9}$$

with λ_k being the eigenvalues of the flux Jacobian. These matrices and eigenvalues are evaluated at some average state.

The dissipation in (3.8) can be written approximately in terms of the jump in the entropy variables, by linearizing the jump in the conserved variables as $\Delta\mathbf{U} = \partial_{\mathbf{V}}\mathbf{U}\Delta\mathbf{V}$, where the Jacobian $\partial_{\mathbf{V}}\mathbf{U}$ is symmetric positive definite [44]. The eigenvector rescaling theorem of Barth [4] ensures the existence of a scaling of the eigenvectors $\mathbf{R} \to \widetilde{\mathbf{R}}$, such that $\partial_{\mathbf{V}}\mathbf{U} = \widetilde{\mathbf{R}}\widetilde{\mathbf{R}}^\top$. The Roe-type flux can thus be re-written as

$$\mathbf{F}_{ij} = \frac{1}{2}\left(\mathbf{f}(\mathbf{U}_i,\mathbf{n}_{ij}) + \mathbf{f}(\mathbf{U}_j,\mathbf{n}_{ij})\right) - \frac{1}{2}\widetilde{\mathbf{R}}_{ij}\mathbf{\Lambda}_{ij}\widetilde{\mathbf{R}}_{ij}^\top\Delta\mathbf{V}_{ij}.$$

This motivates us to choose the *Roe-type* diffusion operator [16]

$$\mathbf{D}_{ij} = \widetilde{\mathbf{R}}_{ij}\mathbf{\Lambda}_{ij}\widetilde{\mathbf{R}}_{ij}^\top \tag{3.10}$$

which is clearly symmetric positive semi-definite. For convenience we will drop the $\widetilde{(.)}$ notation for the remainder of this paper, where it will be understood that $\mathbf{R}_{ij}$ denotes the scaled eigenvectors. The matrices are evaluated at some average state depending on $\mathbf{U}_i$ and $\mathbf{U}_j$. The specific form of the matrices chosen for the Euler equations are described in Appendix A.

Remark 3.2. The Roe type dissipation operator, as chosen above, is just one of a whole host of alternatives when it comes to the choice of numerical dissipation operators [16]. In particular, we can choose $\mathbf{\Lambda} = \max_i |\lambda_i| \mathbf{I}$ to obtain a Rusanov type diffusion operator. Further examples of polynomial viscosity operators are provided in [16].

The dissipation of (numerical) entropy, especially near shocks, is of vital importance from the point of view of quality of the solution profile. The solution near shocks is oscillatory or smeared out, if the entropy content in the shock is too high or too low respectively. To ensure the correct rate of entropy dissipation, Roe and Ismail [24] have introduced the notion of *entropy consistency*, and suggested the following modification of the dissipation operator for the Euler equations

$$\mathbf{\Lambda}_{ij}^{mod} = \mathbf{\Lambda}_{ij} + \alpha_{EC} \tilde{\mathbf{\Lambda}}_{ij}, \qquad \tilde{\mathbf{\Lambda}}_{ij} = \mathrm{diag}\Big(\Delta(u_n - a)_{ij}, 0, 0, \Delta(u_n + a)_{ij}\Big). \tag{3.11}$$

Based on weak shock assumptions, the value $\alpha_{EC} = 1/6$ has been suggested in [24].

3.4 High-order diffusion operators

For smooth solutions $\Delta \mathbf{V}_{ij} = \mathcal{O}(|\Delta \mathbf{x}_{ij}|)$ so that the diffusion term in schemes of the form (3.7) is just first-order accurate. The first-order scheme is a consequence of taking the solution to be constant in each cell and equal to the cell average value. In order to obtain a higher-order scheme, we need to appropriately reconstruct the solution to the cell interfaces. Consider the cell interface between two control volumes C_i and C_j. Corresponding to this particular cell interface, let $\mathbf{V}_{ij}$ and $\mathbf{V}_{ji}$ be the reconstructed values of $\mathbf{V}$ from cell C_i and C_j respectively, and define the jump at the interface by

$$[\![\mathbf{V}]\!]_{ij} = \mathbf{V}_{ji} - \mathbf{V}_{ij}. \tag{3.12}$$

We will use the above higher-order jump in the numerical flux (3.7) instead of $\Delta \mathbf{V}_{ij}$. If the reconstruction is exact for affine functions, then $[\![\mathbf{V}]\!]_{ij} = \mathcal{O}(\Delta \mathbf{x}_{ij})^2$ for smooth functions. The following lemma (proved for Cartesian meshes in [16]) gives sufficient conditions on the reconstruction which ensures that the entropy stability of the scheme is preserved.

Lemma 3.2. *For each pair of vertices (i,j) which are connected to one another, let $\mathbf{R}_{ij}$ be non-singular, let $\mathbf{\Lambda}_{ij}$ be any non-negative diagonal matrix, and define the numerical diffusion matrix*

$$\mathbf{D}_{ij} = \mathbf{R}_{ij} \mathbf{\Lambda}_{ij} \mathbf{R}_{ij}^\top.$$

Let $\mathbf{V}_{ij}$ and $\mathbf{V}_{ji}$ be the reconstructed values of the entropy variables at the interface between C_i and C_j respectively. Assume that the reconstruction ensures the existence of a diagonal matrix $\mathbf{B}_{ij} \geqslant 0$ such that

$$[\![\mathbf{V}]\!]_{ij} = \left(\mathbf{R}_{ij}^\top\right)^{-1} \mathbf{B}_{ij} \mathbf{R}_{ij}^\top \Delta \mathbf{V}_{ij}. \tag{3.13}$$

Then the scheme with the numerical flux

$$\mathbf{F}_{ij} = \mathbf{F}_{ij}^* - \frac{1}{2} \mathbf{D}_{ij} [\![\mathbf{V}]\!]_{ij} \tag{3.14}$$

is entropy stable with numerical entropy flux

$$q_{ij} := q_{ij}^* - \frac{1}{2} \overline{\mathbf{V}}_{ij}^\top \mathbf{D}_{ij} [\![\mathbf{V}]\!]_{ij}.$$

Proof. As in the proof of Lemma 3.1, consider (2.1) with the flux defined by (3.14) and multiply it by the entropy variables $\mathbf{V}_i$ to get

$$\begin{aligned}
\frac{\mathrm{d}}{\mathrm{d}t} \eta(\mathbf{U}_i) &= -\frac{1}{|C_i|} \sum_{j \in i} \mathbf{V}_i^\top \mathbf{F}_{ij} \\
&= -\frac{1}{|C_i|} \sum_{j \in i} q_{ij}^* + \frac{1}{2|C_i|} \sum_{j \in \mathcal{N}_i} \left[\left(\overline{\mathbf{V}}_{ij} - \frac{1}{2} \Delta \mathbf{V}_{ij} \right)^\top \mathbf{D}_{ij} [\![\mathbf{V}]\!]_{ij} \right] \\
&= -\frac{1}{|C_i|} \sum_{j \in i} \left[q_{ij}^* - \frac{1}{2} \overline{\mathbf{V}}_{ij}^\top \mathbf{D}_{ij} [\![\mathbf{V}]\!]_{ij} \right] - \frac{1}{4|C_i|} \sum_{j \in i} \Delta \mathbf{V}_{ij}^\top \mathbf{R}_{ij} \mathbf{\Lambda}_{ij} \mathbf{B}_{ij} \mathbf{R}_{ij}^\top \Delta \mathbf{V}_{ij}.
\end{aligned}$$

Since $\mathbf{R}_{ij} \mathbf{\Lambda}_{ij} \mathbf{B}_{ij} \mathbf{R}_{ij}^\top$ is symmetric positive semi-definite, we get

$$\frac{\mathrm{d}}{\mathrm{d}t} \eta(\mathbf{U}_i) + \frac{1}{|C_i|} \sum_{j \in i} q_{ij} \leqslant 0.$$

This completes the proof. □

Remark 3.3. The quantities $\mathbf{R}_{ij}$, $\mathbf{\Lambda}_{ij}$ are evaluated at some average value corresponding to $\mathbf{V}_i$, $\mathbf{V}_j$. Note that $\mathbf{F}_{ij}^* = \mathbf{F}^*(\mathbf{V}_i, \mathbf{V}_j, \mathbf{n}_{ij})$, i.e., it is evaluated using the solution at the vertices and only the dissipation flux makes use of the reconstructed values. Since both $\mathbf{F}_{ij}^*$ and the dissipation flux are second-order accurate, the numerical flux $\mathbf{F}_{ij}$ is also second-order accurate for smooth solutions.

3.4.1 Reconstruction procedure

In order to use Lemma 3.2, we describe a reconstruction procedure that satisfies (3.13). For each cell interface described by the neighbouring vertices i and j, define the *scaled entropy variables* $\mathbf{Z} = \mathbf{R}_{ij}^\top \mathbf{V}$. Let $\mathbf{Z}_{ij}$, $\mathbf{Z}_{ji}$ be the reconstructed values of $\mathbf{Z}$ at the interface from cell C_i and C_j respectively. Then define

$$\mathbf{V}_{ij} = (\mathbf{R}_{ij}^\top)^{-1} \mathbf{Z}_{ij}, \qquad \mathbf{V}_{ji} = (\mathbf{R}_{ij}^\top)^{-1} \mathbf{Z}_{ji} \qquad \Longrightarrow \qquad [\![\mathbf{V}]\!]_{ij} = (\mathbf{R}_{ij}^\top)^{-1} [\![\mathbf{Z}]\!]_{ij}.$$

Thus, the dissipation terms in the flux given by (3.14) can be written in terms of the scaled entropy variables as

$$\mathbf{D}_{ij}[\![\mathbf{V}]\!]_{ij} = \mathbf{R}_{ij}\boldsymbol{\Lambda}_{ij}[\![\mathbf{Z}]\!]_{ij}.$$

The condition given by (3.13) can now be interpreted in terms of the scaled variables as

$$[\![\mathbf{Z}]\!]_{ij} = \mathbf{B}_{ij}\Delta\mathbf{Z}_{ij}$$

for some diagonal matrix $\mathbf{B}_{ij}$ with non-negative entries. Componentwise, this further reduces to a *sign property* on the n different components of $\mathbf{Z}$:

$$\operatorname{sign}\Big([\![\mathbf{Z}]\!]_{ij}\Big) = \operatorname{sign}\Big(\Delta\mathbf{Z}_{ij}\Big). \tag{3.15}$$

We now describe a slope-limited linear reconstruction procedure of scaled entropy variables appearing in the dissipation terms, which satisfies the sign property. For neighbouring control volumes C_i and C_j, the scaled entropy variables with respect to the interface between nodes i and j are given by

$$\mathbf{Z}_i = \mathbf{R}_{ij}^\top \mathbf{V}_i, \qquad \mathbf{Z}_j = \mathbf{R}_{ij}^\top \mathbf{V}_j. \tag{3.16}$$

In order to perform the reconstruction we need more information along the line joining vertices i and j so that we can get some information about the smoothness of the function. Let us extend the line by an equal length on either side to obtain the additional nodes $i-1$ and $j+1$ (Fig. 4(a)). If the values $\mathbf{Z}_{i-1}$, $\mathbf{Z}_{j+1}$ are known, then define following differences

- The forward differences

$$\Delta_{ij}^f = \Delta\mathbf{Z}_{ij}, \qquad \Delta_{ji}^f = \mathbf{Z}_{j+1} - \mathbf{Z}_j. \tag{3.17}$$

- The backward differences

$$\Delta_{ij}^b = \mathbf{Z}_i - \mathbf{Z}_{i-1}, \qquad \Delta_{ji}^b = \Delta\mathbf{Z}_{ij}. \tag{3.18}$$

The reconstructed values of $\mathbf{Z}$ at the interface are given by

$$\mathbf{Z}_{ij} = \mathbf{Z}_i + \frac{1}{2}\mathcal{M}\left(\Delta_{ij}^f, \Delta_{ij}^b\right), \qquad \mathbf{Z}_{ji} = \mathbf{Z}_j - \frac{1}{2}\mathcal{M}\left(\Delta_{ji}^f, \Delta_{ji}^b\right), \tag{3.19}$$

where we have used the minmod slope limiter function

$$\mathcal{M}(a,b) = \begin{cases} s\min(|a|,|b|) & \text{if} \quad s := \operatorname{sign}(a) = \operatorname{sign}(b), \\ 0 & \text{otherwise.} \end{cases}$$

There are several methods available in the literature to obtain the additional information $\mathbf{Z}_{i-1}$ and $\mathbf{Z}_{j+1}$, which need not correspond to actual points in the mesh.

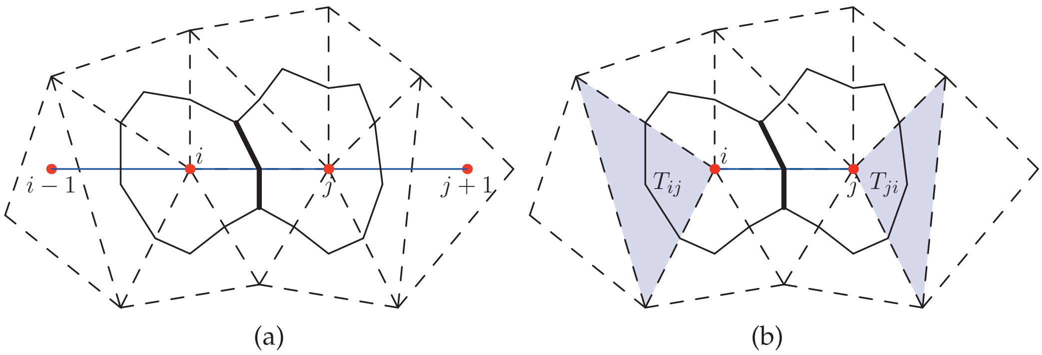

Figure 4: Stencil for linear reconstruction (a) extension and interpolation, (b) extension into upstream/downstream triangles.

- The values at the nodes $i-1$ and $j+1$ can be evaluated through continuation and interpolation from neighbouring nodes [6], as shown in Fig. 4(a).
- The differences Δ^b_{ij} and Δ^f_{ji} can be estimated if we know the gradients of $\mathbf{Z}$ at the nodes [50].
- For the edge joining the nodes i and j, one considers the *upstream* and *downstream* triangles T_{ij} and T_{ji} through which the extended edge would pass (see Fig. 4(b)). The gradients evaluated on these triangles can be used instead of nodal gradients [3,6,39].

In our reconstruction procedure, we shall use nodal gradients to evaluate the differences as follows.

$$\Delta^f_{ji}=\mathbf{Z}_{j+1}-\mathbf{Z}_j=2\nabla_h\mathbf{Z}_j\cdot(\mathbf{x}_j-\mathbf{x}_i)-\Delta\mathbf{Z}_{ij}, \tag{3.20}$$

$$\Delta^b_{ij}=\mathbf{Z}_i-\mathbf{Z}_{i-1}=2\nabla_h\mathbf{Z}_i\cdot(\mathbf{x}_j-\mathbf{x}_i)-\Delta\mathbf{Z}_{ij}. \tag{3.21}$$

The procedure used to approximate the gradients at the nodes, is described in Section 3.4.2.

Lemma 3.3. *The reconstruction of the scaled entropy variables described by* (3.19), (3.17) *and* (3.18) *satisfies the sign property* (3.15).

Proof. For any component Z of $\mathbf{Z}$, the reconstruction scheme gives

$$Z_{ji}-Z_{ij}=(Z_j-Z_i)-\frac{1}{2}\left[\mathcal{M}\left(\Delta^f_{ji},\Delta^b_{ji}\right)+\mathcal{M}\left(\Delta^f_{ij},\Delta^b_{ij}\right)\right].$$

If $Z_j-Z_i\geqslant 0$, then

$$\mathcal{M}\left(\Delta^f_{ij},\Delta^b_{ij}\right)\leqslant\Delta^f_{ij},\qquad \mathcal{M}\left(\Delta^f_{ji},\Delta^b_{ji}\right)\leqslant\Delta^b_{ji}=\Delta^f_{ij}.$$

Thus,

$$Z_{ji}-Z_{ij}\geqslant(Z_j-Z_i)-\frac{1}{2}\left[2\Delta^f_{ij}\right]=0.$$

Similarly, if $Z_j - Z_i \leqslant 0$, then

$$\mathcal{M}\left(\Delta^f_{ij}, \Delta^b_{ij}\right) \geqslant \Delta^f_{ij}, \qquad \mathcal{M}\left(\Delta^f_{ji}, \Delta^b_{ji}\right) \geqslant \Delta^b_{ji} = \Delta^f_{ij}$$

giving us

$$Z_{ji} - Z_{ij} \leqslant (Z_j - Z_i) - \frac{1}{2}\left[2\Delta^f_{ij}\right] = 0.$$

Hence, the reconstruction satisfies the sign property. □

Remark 3.4. The above reconstruction with the minmod limiter is one possible option which has the sign property. One could instead use the second-order ENO scheme (ENO-2), which also satisfies the sign property. Note that the ENO-2 scheme reduces to the minabs limiter. Numerical tests have yielded almost indistinguishable results with both minmod and ENO-2 reconstruction. Thus, we adhere to presenting results with the minmod limiter.

Remark 3.5. Either of the reconstruction methods described above would lead to the sign property, when used with the minmod or minabs limiter. What is crucial to obtain the sign property is that we evaluate $\Delta^f_{ij} = \Delta^b_{ji} = \Delta \mathbf{Z}_{ij}$.

3.4.2 Computation of gradients

The second-order limited reconstruction described above requires the evaluation of nodal gradients of scaled entropy variables. We evaluate these gradient as

$$\nabla_h \mathbf{Z}_i = \mathbf{R}^\top_{ij} \nabla_h \mathbf{V}_i, \tag{3.22}$$

where $\nabla_h \mathbf{V}_i$ must be numerically approximated. Consider the node i and the set of neighbouring primary triangular cells denoted by $T \in i$, as shown in Fig. 5. Using the Green's

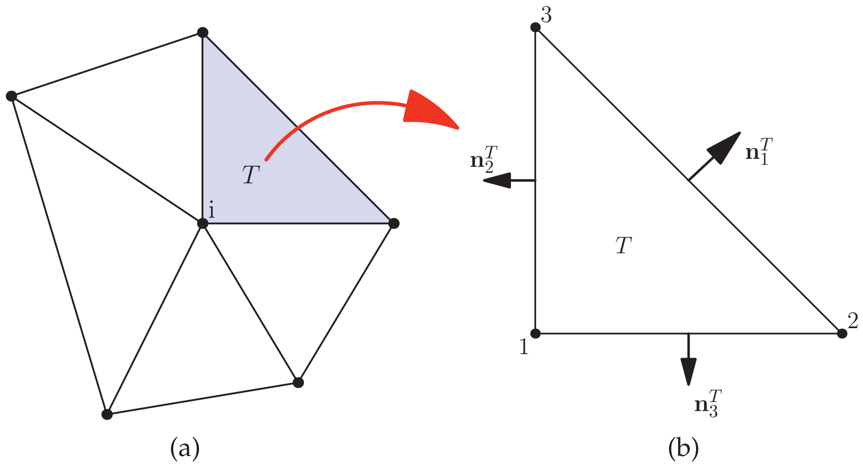

Figure 5: (a) Stencil for gradient evaluation at node i, (b) neighbouring triangle T.

theorem combined with trapezoidal rule for integration [1,12], the gradient on each triangle T is approximated by

$$\nabla_h \mathbf{V}^T = -\frac{1}{2|T|}\Big(\mathbf{V}_1 \otimes \mathbf{n}_1^T + \mathbf{V}_2 \otimes \mathbf{n}_2^T + \mathbf{V}_3 \otimes \mathbf{n}_3^T\Big), \tag{3.23}$$

where $\mathbf{X}\otimes\mathbf{Y} = (\mathbf{X}_m \mathbf{Y}_n)_{m,n}$ denotes the outer product. This approximation is exact for affine functions, and thus second-order accurate. Finally, the gradient at node i is approximated as

$$\nabla_h \mathbf{V}_i = \frac{\sum\limits_{T\in i} |T| \nabla_h \mathbf{V}^T}{\sum\limits_{T\in i} |T|} \tag{3.24}$$

which is exact for affine functions and hence is second-order accurate.

Remark 3.6. In actual implementation of the scheme, we never compute $\mathbf{V}_{ij}$, $\mathbf{V}_{ji}$ which would be expensive since it requires the inversion of the matrix $\mathbf{R}_{ij}$. The numerical flux can be directly computed as

$$\mathbf{F}_{ij} = \mathbf{F}_{ij}^* - \frac{1}{2}\mathbf{R}_{ij}\mathbf{\Lambda}_{ij}\left(\mathbf{Z}_{ji} - \mathbf{Z}_{ij}\right) \tag{3.25}$$

thus avoiding some costly operations.

Remark 3.7. One could also approximate $\nabla_h \mathbf{Z}_i$ and $\nabla_h \mathbf{Z}^T$ directly from the scaled entropy variables at each node. Since the scaling depends on the particular dual mesh interface at which the reconstruction is being performed, this would require the computation of several nodal and triangular gradients for each node and triangle. In order to avoid this additional computational cost and storage requirement, we simply scale the gradients evaluated for the original entropy variables, as given by (3.22).

4 Numerical results

We now present the numerical results of the scheme discussed above on several standard two dimensional test cases. We introduce the following nomenclature for various schemes that are tested in this section. The base scheme shall be the kinetic energy preserving and entropy conservative scheme from Example 3.2.

- **KEPES**: The base scheme with first-order entropy variable based dissipation operator. This corresponds to the scheme (3.7) with the dissipation operator given by (3.9) and (3.10).
- **KEPES-TeCNO**: The base with second-order limited reconstruction of the scaled entropy variables. The scheme has the form given by (3.25) with the reconstructed (limited) states chosen in accordance to (3.19).

- **KEPES2**: The scheme (3.25) with a pure second-order reconstruction of the scaled entropy variables without limiting

$$Z_{ij} = Z_i + \frac{1}{2}\nabla_h Z_i \cdot (\mathbf{x}_j - \mathbf{x}_i), \qquad Z_{ji} = Z_j - \frac{1}{2}\nabla_h Z_j \cdot (\mathbf{x}_j - \mathbf{x}_i).$$

Note that KEPES2 is not necessarily entropy stable as the unlimited reconstruction need not satisfy the sign property. The numerical results are also compared with the results obtained using the original Roe scheme [38].

The semi-discrete scheme is integrated in time using the explicit Strong Stability Preserving Runge-Kutta 3-stage scheme (SSP-RK3) method [21]. The Lower-Upper Symmetric Gauss Seidel method (LU-SGS) [7] is used for implicit time integration, and is preferred for steady problems as it allows larger time steps. In all test cases we consider the ideal gas with $\gamma = 1.4$ except when indicated otherwise. Additionally, we define the Mach number of the flow as $M = a/|\mathbf{u}|$, where $a = \sqrt{\gamma p/\rho}$ is the speed of sound in air. The Mach number is used to describe various flow regimes: the flow is *subsonic* for $M<1$, *supersonic* for $M>1$ and *transonic* if the flow has both supersonic and subsonic regions.

4.1 Modified shock tube problem

This test case describes a shock tube problem of the Sod type [41]. The primary and the Voronoi dual meshes used for the simulations are shown in Fig. 6. We consider a rectangular domain $[0,1]\times[0,0.4]$ and discretize it with 100 nodes in the direction of the flow, and 80 nodes along the flow cross-section. The left state is given by $(\rho_L, u_L, v_L, p_L) = (1.0, 0.75, 0.0, 1.0)$ and the right state is given by $(\rho_R, u_R, v_R, p_R) = (0.125, 0.0, 0.0, 0.1)$, with the initial discontinuity along $x = 0.3$. Time integration is performed using SSP-RK3 with CFL=0.3.

The Roe scheme gives an entropy violating jump in the expansion region where the flow becomes sonic, as shown in Fig. 7. This is not surprising as we have not added any entropy fix to the standard Roe scheme [38]. However, both the KEPES and KEPES-TeCNO schemes, being entropy stable, are able to remedy this issue to a large extent. The comparison in Fig. 8 shows that the high-resolution KEPES-TeCNO scheme is significantly more accurate as compared to KEPES. Convergence is demonstrated in Fig. 9, where the solutions are evaluated using KEPES-TeCNO on three levels of uniform grid refinements, with the number of vertices along the streamwise direction being $N = 100$, 200 and 400 respectively.

Note that KEPES and KEPES-TeCNO also give rise to a small jump near the sonic point, which reduces with mesh refinement unlike the jump observed with the Roe scheme (without entropy fix). This jump could be attributed to the absence of the right amount of dissipation. Using the entropy consistent modification (3.11) can fix this issue, as can be seen in Figs. 10 and 11. Focusing on the region near the sonic point in Figs. 10(b) and 10(b), we can observe that for $\alpha_{EC} = 1/6$ the jump reduces drastically.

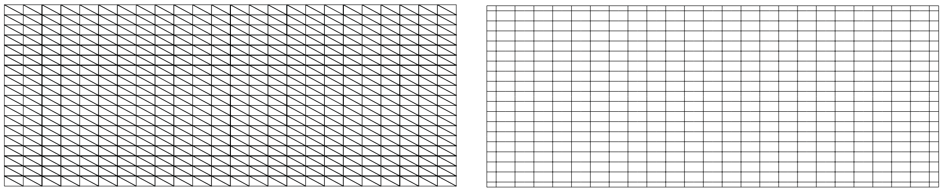

(a) Primal grid (b) Voronoi dual grid

Figure 6: Grid used for shock tube problem.

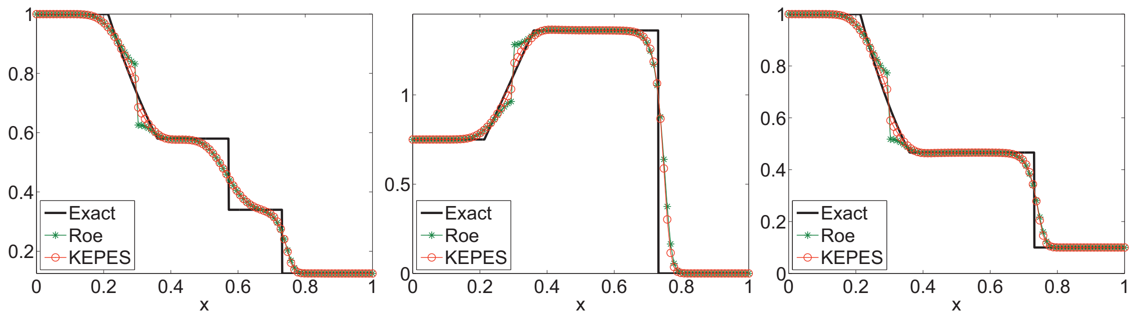

(a) Density (b) x-velocity (c) Pressure

Figure 7: Modified shock tube problem using first-order schemes.

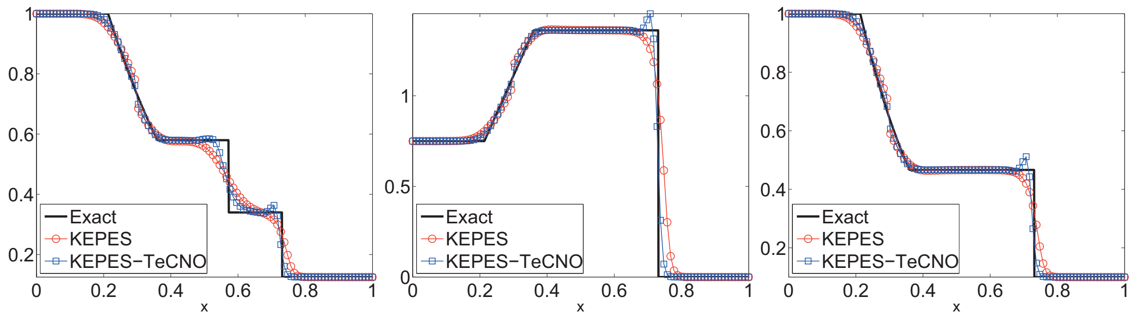

(a) Density (b) x-velocity (c) Pressure

Figure 8: Comparison of KEPES and KEPES-TeCNO schemes.

4.2 Supersonic flow over wedge

This test case involves a weak oblique shock which occurs when a supersonic flow is 'turned into itself' due to the presence of a wedge. The wedge is inclined at an angle of 10 degrees to the horizontal. The farfield Mach number is 2, with slip boundary conditions on the wedge. The mesh (see Fig. 12) has 18848 nodes and we use median dual cells as control volumes. Time integration is performed using LU-SGS. As can be seen in Fig. 13, the shock profile is quite dissipated with KEPES. But, the minmod reconstruction in KEPES-TeCNO scheme leads to a much sharper shock profile, that is comparable to

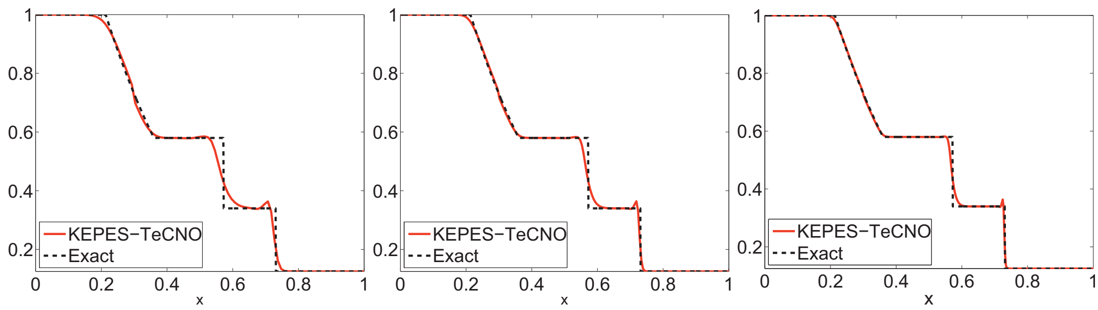

(a) $N=100$ (b) $N=200$ (c) $N=400$

Figure 9: Density plot; grid refinement study with KEPES-TeCNO.

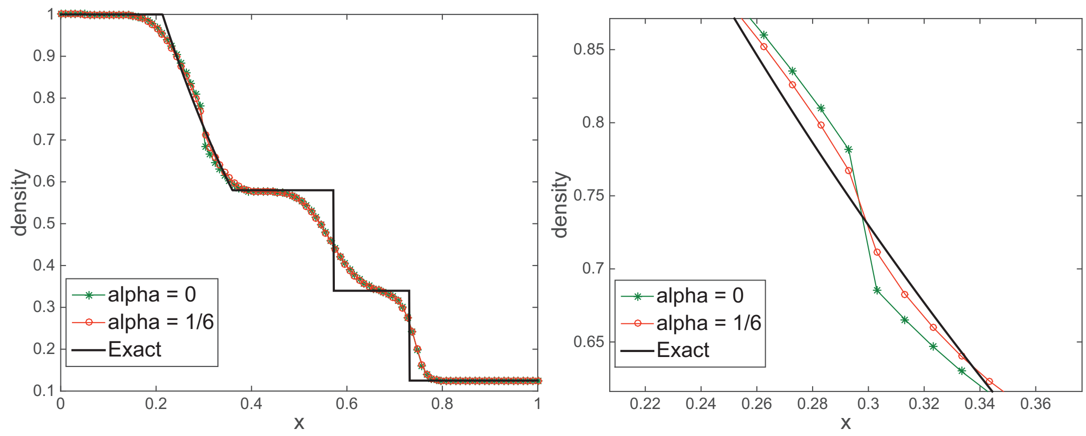

Figure 10: Density plot for $N=100$ and the KEPES scheme, with the entropy consistent modification.

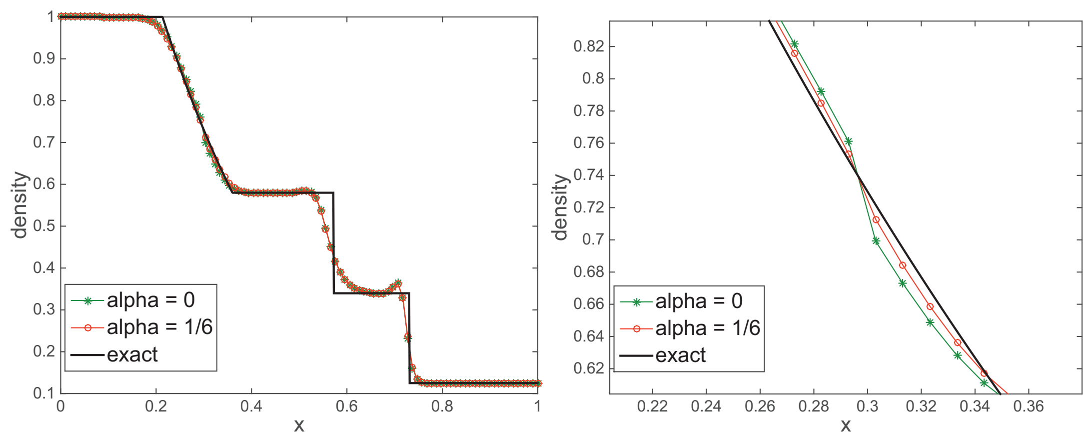

Figure 11: Density plot for $N=100$ and the KEPES-TeCNO scheme, with the entropy consistent modification.

the one computed by the Roe scheme with MUSCL type reconstruction and van Albada limiter [45].

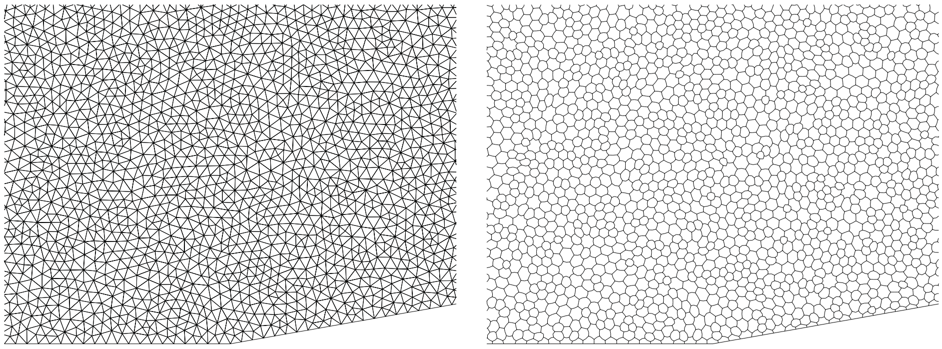

(a) Primary (b) Median dual

Figure 12: Mesh for flow over wedge.

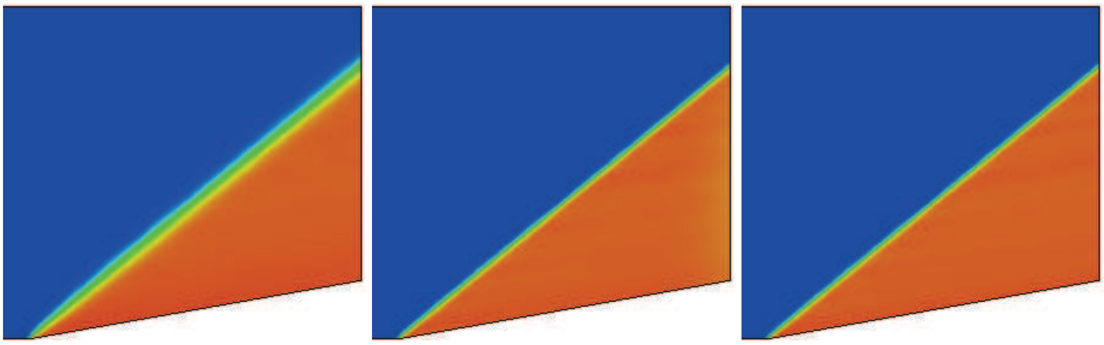

(a) KEPES (b) KEPES-TeCNO (c) Roe (MUSCL)

Figure 13: Mach number plots for a supersonic flow past a wedge.

4.3 Transonic flow past NACA-0012 airfoil

This is an example of a symmetric NACA-0012 airfoil placed in a free-stream Mach number of 0.85 and angle of attack of 2 degrees. The primary mesh and the corresponding median dual mesh used for this test case are shown in Fig. 14. The flow develops shocks both on the upper and lower airfoil surfaces. We compute this flow on a triangular grid by considering the median dual cells, containing 180 points on the airfoil surface and 20 points on the farfield boundary which is a circle, with a total of 6402 vertices. Time integration is performed using LU-SGS. The Mach contour plots in Fig. 15 show that KEPES-TeCNO gives much better shock resolution than KEPES, and comparable to the high-resolution Roe-MUSCL scheme.

The pressure coefficient for compressible flows is given by

$$C_p = \frac{2}{\gamma M_\infty^2}\left(\frac{p}{p_\infty} - 1\right),$$

where p is the nodal pressure, while p_∞ and M_∞ are the farfield pressure and Mach

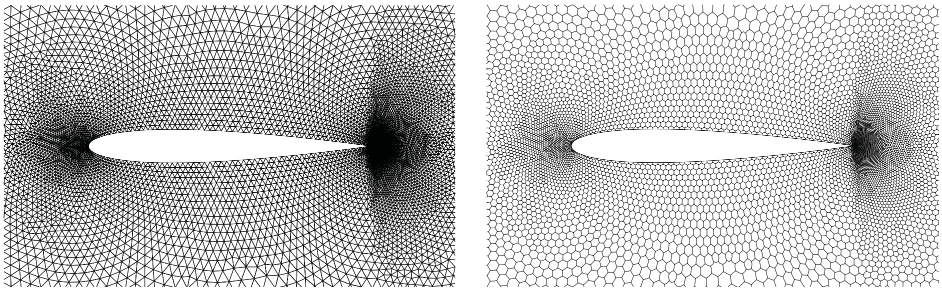

(a) Primary (b) Median dual

Figure 14: Mesh for flow past NACA-0012 airfoil.

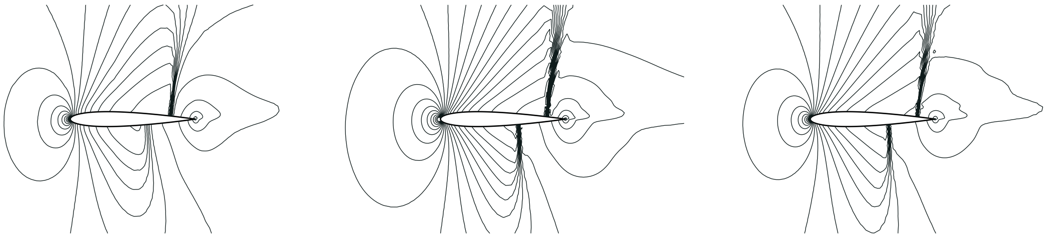

(a) KEPES (b) KEPES-TeCNO (c) Roe (MUSCL)

Figure 15: Mach number, 30 equally spaced contours between 0.04 and 1.7.

numbers respectively. We consider the nodal values of C_p on the surface of the airfoil, as shown in Fig. 16. The x-axis represents the normalized wingspan, while the y-axis represents the inverted pressure coefficient. Thus, the upper surface of the wing, which has a much lower pressure distribution as compared to the lower surface, appears at the top of the plot. There is a sudden change in pressure across the shock that develops on both surfaces, and is clearly visible in the C_p plots. The area enclosed by the graph in the plots represents the lift experienced by the airfoil. Again, the high resolution KEPES-TeCNO was indistinguishable in accuracy with the standard high resolution Roe-MUSCL scheme.

4.4 Supersonic flow past cylinder

Most shock-capturing numerical schemes, except for a few highly dissipative schemes like the Rusanov scheme, can lead to numerical instabilities, particularly when approximating strong shocks. One of the most common anomalies is the *carbuncle phenomenon* [36, 37], which is produced when computing a supersonic flow past a blunt body such as a circular cylinder. Instead of having a smooth bow shock profile upstream of the cylinder, a protuberance appears ahead of the bow shock along the stagnation line. This effect seems to be more pronounced the more closely the grid is aligned to the bow shock.

Simulations were performed for the inviscid supersonic flow over a semi-cylinder.

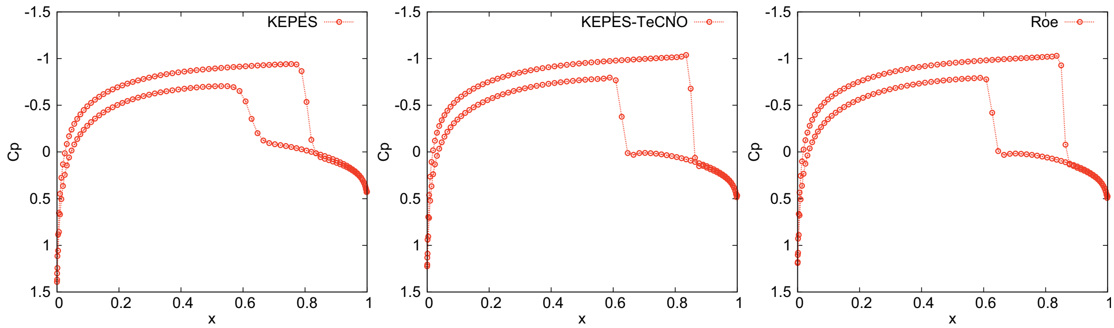

(a) KEPES (b) KEPES-TeCNO (c) Roe (MUSCL)

Figure 16: Pressure coefficient plots of the surface of the airfoil with $p_\infty = 0.9886$, $M_\infty = 0.85$.

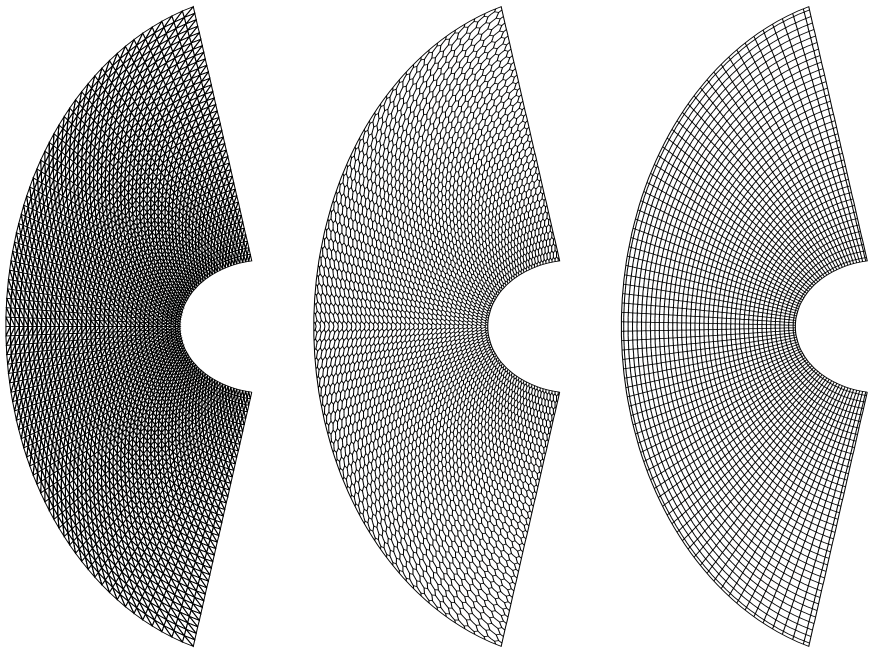

(a) Primal grid (b) Median dual grid (c) Voronoi dual grid

Figure 17: Grid used for supersonic cylinder problem.

The primal triangular grid and the corresponding median and Voronoi dual meshes are shown in Fig. 17. The Voronoi cells lead to nearly structured type grids and can thus lead to carbuncle problem since the shock will be aligned with the cell faces to a greater extent than for the median dual cells. At free-stream Mach number $M_\infty = 2$, KEPES and KEPES-TeCNO give carbuncle free solutions on both median dual and Voronoi dual meshes, as can be seen in Fig. 18. The bow shock is well resolved in each case. Similar results were observed when the schemes were used to simulate an almost hypersonic flow with $M_\infty = 20$, as shown in Fig. 19.

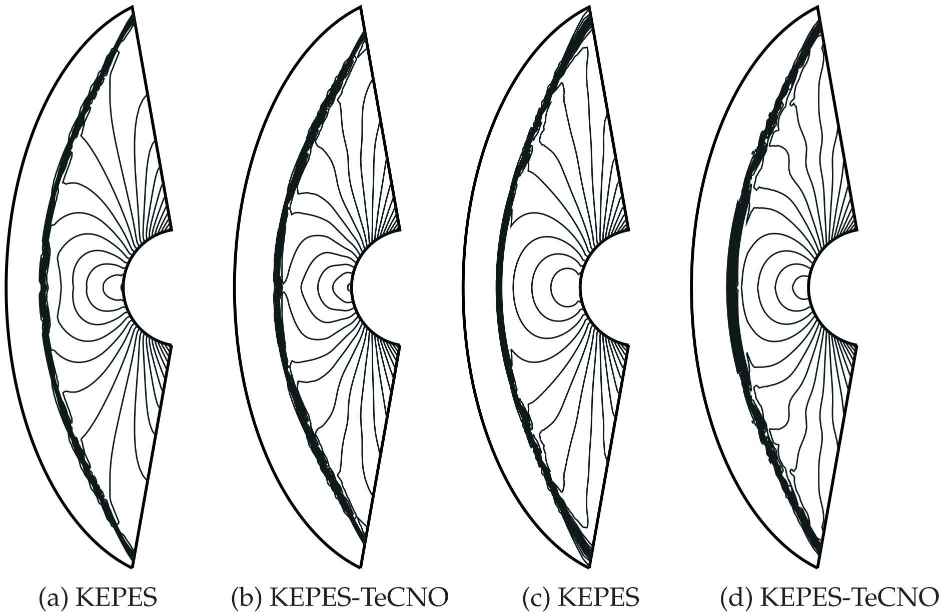

Figure 18: Density contours for supersonic cylinder, $M_\infty = 2$. (a)-(b) median dual grid; (c)-(d) Voronoi dual grid.

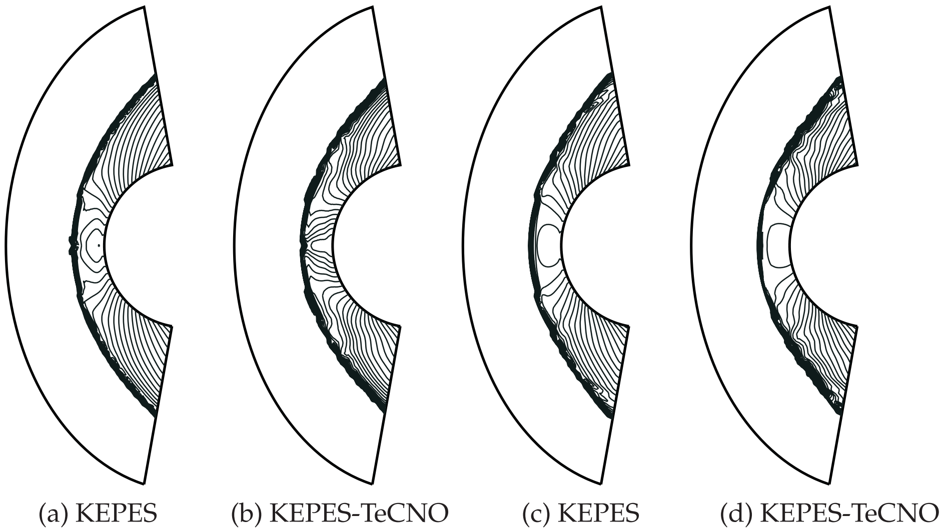

Figure 19: Density contours for supersonic cylinder, $M_\infty = 20$. (a)-(b) median dual grid; (c)-(d) Voronoi dual grid.

4.5 Subsonic flow past cylinder

We consider an inviscid flow past a full cylinder at a low Mach number of 0.3. The mesh used for this problem is shown in Fig. 20. The steady state solution has both top-bottom

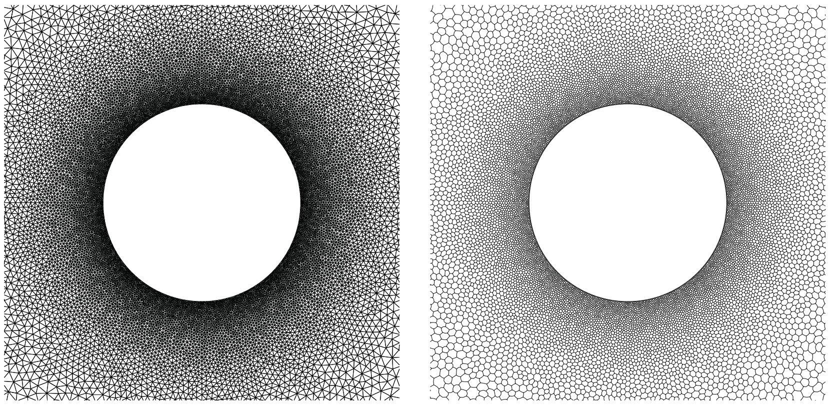

(a) Primary (b) Median dual

Figure 20: Mesh for a subsonic flow past a cylinder.

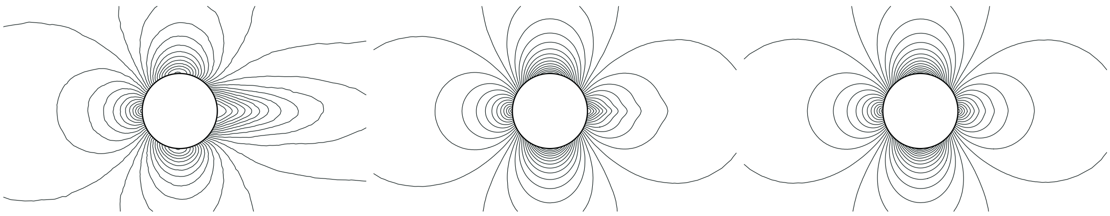

(a) KEPES (b) KEPES-TeCNO (c) KEPES2

Figure 21: Mach number, 30 equally spaced contours between 0.001 and 0.7.

and left-right symmetry. The first-order KEPES solution loses its symmetry due to the excessive dissipation, as shown in Fig. 21. The KEPES-TeCNO does a much better job at preserving the symmetry property, comparable to the approximate solution given by the unlimited second-order KEPES2 scheme.

The flow under consideration is nearly isentropic, that is, the physical entropy of the flow around the cylinder should be nearly constant. To demonstrate the ability of the schemes to preserve this constancy, the entropy bounds obtained with each scheme and their percentage deviation from the free-stream entropy value are mentioned in Table 1. We notice that KEPES gives the largest positive deviation, KEPES2 gives almost negligible positive deviation, while the limited KEPES-TeCNO scheme lies somewhere in between. Both the entropy stable schemes show no negative deviations, while the KEPES2 scheme gives almost negligible negative deviation. Although the KEPES2 performs the best in this scenario, we cannot theoretically prove any stability estimates with it. Moreover, the unlimited KEPES2 would perform rather poorly in the presence of shocks.

Table 1: Physical entropy bounds, with free-stream $s_\infty = 2.07147$.

Scheme	Minimum	Maximum	Percent deviation from s_∞	
KEPES	2.07147	2.08695	+0.747 %	-0.000 %
KEPES-TeCNO	2.07147	2.07208	+0.029 %	-0.000 %
KEPES2	2.07139	2.07153	+0.003 %	-0.004 %

4.6 Step in wind tunnel

This test case is described in [51] and involves an inviscid supersonic flow past a step in a wind tunnel which is impulsively started, with initial Mach number $M=3$. The wind tunnel is one unit length wide and three unit lengths long. The step is 0.2 unit length high and is located 0.6 unit length from the left-hand end of the tunnel. At the left boundary, one imposes an inflow boundary condition. The exit boundary condition on the right has no effect on the flow, because the exit velocity is always supersonic. Along the top and bottom walls of the tunnel slip boundary conditions are applied. The corner of the step is the center of a rarefaction fan and hence is a singular point of the flow.

The flow develops several shocks which undergo further reflections. A shock triple point intersection leads to the formation of a slip line. The grid is adapted to be finer near the corner where the spacing is of size ≈ 0.002 while the maximum spacing is of size ≈ 0.01. The total number of grid-points is 70970. A close-up of the mesh near the corner is shown in Fig. 22. The density contours at time $t=4$ are shown in Fig. 23 using the KEPES-TeCNO scheme which is able to resolve the main features of the flow very accurately.

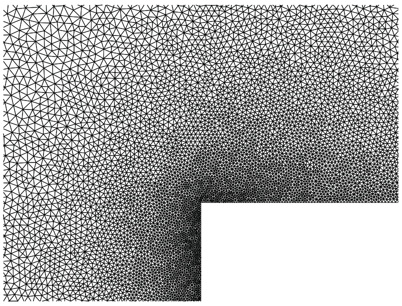

(a) Primary

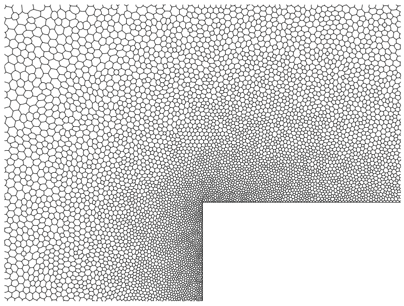

(b) Median dual

Figure 22: Mesh near the corner of the forward step.

5 Conclusions

We consider symmetrizable systems of conservation laws in two space dimensions and design a high-resolution *entropy stable* finite volume scheme to approximate them. The

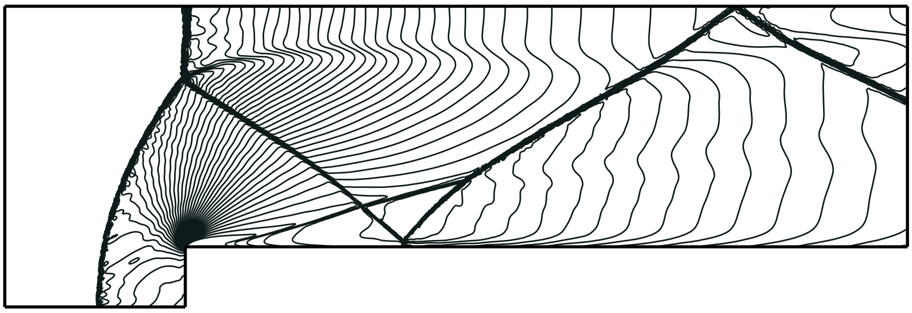

Figure 23: Density, 50 contour lines between 0.5 and 7.1 using KEPES-TeCNO at $t=4$.

underlying computational domain is discretized using triangles and a finite volume scheme is proposed by combining entropy conservative fluxes and numerical dissipation operators, based on piecewise linear reconstruction that enforces a *sign property*. A minmod limiter, satisfying the sign property is used. The resulting scheme is

- Entropy stable i.e, satisfies a discrete form of the entropy inequality. Given that the underlying entropy is strictly convex, the discrete entropy inequality automatically guarantees a bound on the approximate solutions in L^2. To the best of our knowledge, the proposed KEPES-TeCNO scheme is one of the first high-resolution finite volume schemes that are shown to be entropy stable on unstructured grids.
- Robust in approximating complex flow features such as strong (supersonic) shocks, shock reflections, slip lines and near incompressible flows. The robustness of the scheme is demonstrated through a large number of benchmark numerical experiments that illustrate that the KEPES-TeCNO is at least as accurate as a standard high-resolution Roe-MUSCL method.

Thus, we design a scheme whose accuracy is at least comparable to existing high-resolution schemes but at the same time, the proposed scheme has rigorous stability properties. The numerical tests show that the scheme is able to preserve positivity of density and pressure without any additional treatment on unstructured grids. The current scheme is restricted to second-order resolution. Even higher-order schemes are currently being investigated. Future work will present the extension of the proposed methodology to the Navier-Stokes equations and to three space dimensions.

Acknowledgments

This research work benefited from the support of the AIRBUS Group Corporate Foundation Chair in Mathematics of Complex Systems, established in TIFR/ICTS, Bangalore. The research of SM was partly supported by ERC StG NN. 306279 SPARCCLE. SM dedicates this paper to Eitan Tadmor on his 60th birthday.

A Roe-type dissipation for Euler equations

The Roe-type dissipation matrix is given by

$$\mathbf{D}_{ij} = \mathbf{R}_{ij} \mathbf{\Lambda}_{ij} \mathbf{R}_{ij}^{\top},$$

where

$$\begin{aligned}
\mathbf{R} &= \begin{pmatrix} 1 & 1 & 0 & 1 \\ u - a\tilde{n}_1 & u & \tilde{n}_2 & u + a\tilde{n}_1 \\ v - a\tilde{n}_2 & v & -\tilde{n}_1 & v + a\tilde{n}_2 \\ H - au_{\tilde{n}} & \frac{1}{2}|\mathbf{u}|^2 & u\tilde{n}_2 - v\tilde{n}_1 & H + au_{\tilde{n}} \end{pmatrix} \mathbf{S}^{\frac{1}{2}}, \\
\mathbf{S} &= \operatorname{diag}\left(\frac{\rho}{2\gamma}, \quad \frac{(\gamma-1)\rho}{\gamma}, \quad p, \quad \frac{\rho}{2\gamma} \right), \\
\mathbf{\Lambda} &= \operatorname{diag}\left(|u_n - a|, \quad |u_n|, \quad |u_n|, \quad |u_n + a| \right).
\end{aligned}$$

In the above expressions, $\mathbf{S}$ is the scaling matrix for the eigenvectors, $\tilde{\mathbf{n}}$ is the unit outward normal on the faces, $u_{\tilde{n}} = \mathbf{u} \cdot \tilde{\mathbf{n}}$, $a = \sqrt{\gamma p / \rho}$ is the speed of sound in air and $H = a^2/(\gamma - 1) + |\mathbf{u}|^2/2$ is the specific enthalpy. The following average states are used to evaluate the above matrices:

$$\mathbf{u} = \overline{\mathbf{u}}_{ij}, \qquad \rho = \widehat{\rho}_{ij}, \qquad p = \frac{\overline{\rho}_{ij}}{2\overline{\beta}_{ij}}, \qquad a = \sqrt{\frac{\gamma}{2\widehat{\beta}_{ij}}}. \tag{A.1}$$

The KEPES scheme (see Section 4) is able to resolve stationary contact discontinuities exactly, if the speed of sound a in the dissipation operator $\mathbf{D}_{ij}$ evaluated using the expression described in (A.1) [8].

References

[1] W. Kyle Anderson. A grid generation and flow solution method for the euler equations on unstructured grids. *J. Comput. Phys.*, 110(1):23–38, 1994.

[2] F. Angrand and F. C. Lafon. Flux formulation using a fully 2D approximate Roe Riemann solver. In A. Donato and F. Oliveri, editors, *Nonlinear Hyperbolic Problems: Theoretical, Applied, and Computational Aspects*, volume 43 of *Notes on Numerical Fluid Mechanics (NNFM)*, pages 15–22. Vieweg+Teubner Verlag, 1993.

[3] P. Arminjon, A. Dervieux, L. Fezoui, H. Steve, and B. Stoufflet. Non-oscillatory schemes for multidimensional Euler calculations with unstructured grids. In J. Ballmann and R. Jeltsch, editors, *Nonlinear Hyperbolic Equations Theory, Computation Methods, and Applications*, volume 24 of *Notes on Numerical Fluid Mechanics*, pages 1–10. Vieweg+Teubner Verlag, 1989.

[4] T. J. Barth. Numerical methods for gasdynamic systems on unstructured meshes. In *An Introduction to Recent Developments in Theory and Numerics for Conservation Laws (Freiburg/Littenweiler, 1997)*, volume 5 of *Lect. Notes Comput. Sci. Eng.*, pages 195–285. Springer, Berlin, 1999.

[5] T. J. Barth and D. C. Jespersen. The Design and Application of Upwind Schemes on Unstructured Meshes. *AIAA-89-0366*, 1989.

[6] V. Billey, J. Périaux, P. Perrier, and B. Stoufflet. 2-D and 3-D Euler computations with finite element methods in aerodynamics. In *Nonlinear Hyperbolic Problems (St. Etienne, 1986)*, volume 1270 of *Lecture Notes in Math.*, pages 64–81. Springer, Berlin, 1987.

[7] J. Blazek. *Computational Fluid Dynamics: Principles and Applications*. Elsevier Science, Oxford, second edition, 2005.

[8] P. Chandrashekar. Kinetic energy preserving and entropy stable finite volume schemes for compressible Euler and Navier-Stokes equations. *Commun. Comput. Phys.*, 14(5):1252–1286, 2013.

[9] B. Cockburn and C.-W. Shu. TVB Runge-Kutta local projection discontinuous Galerkin finite element method for conservation laws. II. General framework. *Math. Comp.*, 52(186):411–435, 1989.

[10] P. Colella. A direct Eulerian MUSCL scheme for gas dynamics. *SIAM J. Sci. Statist. Comput.*, 6(1):104–117, 1985.

[11] C. M. Dafermos. *Hyperbolic conservation laws in continuum physics*, volume 325 of *Grundlehren der Mathematischen Wissenschaften [Fundamental Principles of Mathematical Sciences]*. Springer-Verlag, Berlin, third edition, 2010.

[12] H. Deconinck, P. L. Roe, and R. Struijs. A multidimensional generalization of Roe's flux difference splitter for the Euler equations. *Comput. & Fluids*, 22(2-3):215–222, 1993.

[13] J.-A. Désidéri and A. Dervieux. Compressible flow solvers using unstructured grids. In *Computational Fluid Dynamics, Vol. 1, 2*, volume 88 of *von Karman Inst. Fluid Dynam. Lecture Ser.*, page 115. von Karman Inst. Fluid Dynamics, Rhode-St-Genèse, 1988.

[14] L. J. Durlofsky, B. Engquist, and S. Osher. Triangle based adaptive stencils for the solution of hyperbolic conservation laws. *J. Comput. Phys.*, 98(1):64–73, 1992.

[15] U. S. Fjordholm, S. Mishra, and E. Tadmor. Energy preserving and energy stable schemes for the shallow water equations. In F. Cucker, A. Pinkus and M. Todd, editors, *Proc. FoCM (Hong Kong, 2008)*, London Math. Soc. Lecture Notes Ser. 363, pages 93–139, 2009.

[16] U. S. Fjordholm, S. Mishra, and E. Tadmor. Arbitrarily high-order accurate entropy stable essentially nonoscillatory schemes for systems of conservation laws. *SIAM J. Numer. Anal.*, 50(2):544–573, 2012.

[17] U. S. Fjordholm. S. Mishra, and E. Tadmor. ENO reconstruction and ENO interpolation are stable. *Foundations of Computational Mathematics* 13(2):139–159, 2013.

[18] U. S. Fjordholm, R. Käppeli, S. Mishra, and E. Tadmor. Construction of approximate entropy measure-valued solutions for hyperbolic systems of conservation laws. *Foundations of Computational Mathematics*, pages 1–65, 2015.

[19] E. Godlewski and P.-A. Raviart. *Numerical Approximation of Hyperbolic Systems of Conservation Laws*, volume 118 of *Applied Mathematical Sciences*. Springer-Verlag, New York, 1996.

[20] S. K. Godunov. An interesting class of quasilinear systems. *Dokl. Akad. Nauk. SSSR*, 139:521–523, 1961.

[21] S. Gottlieb, C.-W. Shu, and E. Tadmor. Strong stability-preserving high-order time discretization methods. *SIAM Rev.*, 43(1):89–112 (electronic), 2001.

[22] A. Harten. On the symmetric form of systems of conservation laws with entropy. *J. Comput. Phys.*, 49(1):151–164, 1983.

[23] T. J. R. Hughes, L. P. Franca, and M. Mallet. A new finite element formulation for computational fluid dynamics. I. Symmetric forms of the compressible Euler and Navier-Stokes equations and the second law of thermodynamics. *Comput. Methods Appl. Mech. Engrg.*, 54(2):223–234, 1986.

[24] F. Ismail and P. L. Roe. Affordable, entropy-consistent Euler flux functions II: Entropy pro-

duction at shocks. *J. Comput. Phys.*, 228(15):5410–5436, 2009.

[25] A. Jameson, W. Schmidt, and E. Turkel. Numerical Solution of the Euler Equations by Finite Volume Methods Using Runge-Kutta Time-Stepping Schemes. In *AIAA Paper 1981-1259*, page 1, 1981.

[26] A. Jameson and D. Mavriplis. Finite volume solution of the two-dimensional Euler equations on a regular triangular mesh. *AIAA Journal*, 24:611–618, 1986.

[27] A. Jameson. Formulation of kinetic energy preserving conservative schemes for gas dynamics and direct numerical simulation of one-dimensional viscous compressible flow in a shock tube using entropy and kinetic energy preserving schemes. *J. Sci. Comput.*, 34(2):188–208, 2008.

[28] A. Katz and V. Sankaran. An efficient correction method to obtain a formally third-order accurate flow solver for node-centered unstructured grids. *J. Sci. Comput.*, 51(2):375–393, 2012.

[29] D. Kröner, S. Noelle, and M. Rokyta. Convergence of higher order upwind finite volume schemes on unstructured grids for scalar conservation laws in several space dimensions. *Numerische Mathematik*, 71(4):527–560, 1995.

[30] D. Kröner and M. Rokyta. Convergence of upwind finite volume schemes for scalar conservation laws in two dimensions. *SIAM J. Numer. Anal.*, 31(2):324–343, 1994.

[31] P. G. Lefloch, J. M. Mercier, and C. Rohde. Fully discrete, entropy conservative schemes of arbitrary order. *SIAM J. Numer. Anal.*, 40(5):1968–1992 (electronic), 2002.

[32] A. Madrane, U. S. Fjordholm, S. Mishra, and E. Tadmor. Entropy conservative and entropy stable finite volume schemes for multi-dimensional conservation laws on unstructured meshes. Technical Report 2012-31, Seminar for Applied Mathematics, ETH Zürich, 2012.

[33] D. J. Mavriplis. Adaptive mesh generation for viscous flows using delaunay triangulation. *J. Comput. Phys.*, 90(2):271–291, 1990.

[34] M. S. Mock. Systems of conservation laws of mixed type. *J. Differential Equations*, 37(1):70–88, 1980.

[35] B. Perthame and Y. Qiu. A variant of van Leer's method for multidimensional systems of conservation laws. *J. Comput. Phys.*, 112(2):370–381, June 1994.

[36] J.-Ch. Robinet, J. Gressier, G. Casalis, and J.-M. Moschetta. Shock wave instability and the carbuncle phenomenon: Same intrinsic origin? *J. Fluid Mech.*, 417:237–263, 2000.

[37] P.L. Roe, H. Nishikawa, F. Ismail, and L. Scalabrin. On carbuncles and other excrescences. In *17th AIAA Computational Fluid Dynamics Conference (Toronto)*, AIAA Paper 2005-4872, 2005.

[38] P. L. Roe. Approximate Riemann solvers, parameter vectors, and difference schemes. *J. Comput. Phys.*, 43(2):357–372, 1981.

[39] P. Rostand and B. Stoufflet. TVD schemes to compute compressible viscous flows on unstructured meshes. In *Nonlinear Hyperbolic Equations — Theory, Computation Methods, and Applications (Aachen, 1988)*, volume 24 of *Notes Numer. Fluid Mech.*, pages 510–520. Vieweg, Braunschweig, 1989.

[40] C.-W. Shu and S. Osher. Efficient implementation of essentially non-oscillatory shock-capturing schemes. *J. Comput. Phys.*, 77(2):439–471, 1988.

[41] G. A. Sod. A survey of several finite difference methods for systems of nonlinear hyperbolic conservation laws. *J. Comput. Phys.*, 27(1):1–31, 1978.

[42] B. Stoufflet. Implicit finite element methods for the Euler equations. In *Numerical Methods for the Euler Equations of Fluid Dynamics (Rocquencourt, 1983)*, pages 409–434. SIAM, Philadelphia, PA, 1985.

[43] E. Tadmor. Numerical viscosity and the entropy condition for conservative difference schemes. *Math. Comp.*, 43(168):369–381, 1984.

[44] E. Tadmor. Entropy stability theory for difference approximations of nonlinear conservation laws and related time-dependent problems. *Acta Numer.*, 12:451–512, 2003.

[45] G. D. van Albada, B. van Leer, and W. W. Roberts, Jr.. A comparative study of computational methods in cosmic gas dynamics. In M. Y. Hussaini, B. van Leer, and J. Van Rosendale, editors, *Upwind and High-Resolution Schemes*, pages 95–103. Springer Berlin Heidelberg, 1997.

[46] B. van Leer. Towards the ultimate conservative difference scheme. V. A second-order sequel to Godunov's method [*J. Comput. Phys.*, 32(1):101–136, 1979]. *J. Comput. Phys.*, 135(2):227–248, 1997. With an introduction by Ch. Hirsch, Commemoration of the 30th anniversary of J. Comput. Phys..

[47] V. Venkatakrishnan. On the Accuracy of Limiters and Convergence to Steady State Solutions. *AIAA-93-0880*, 1993.

[48] V. Venkatakrishnan. Convergence to steady state solutions of the euler equations on unstructured grids with limiters. *J. Comput. Phys.*, 118(1):120–130, 1995.

[49] G. Vijayasundaram. Transonic flow simulations using an upstream centered scheme of Godunov in finite elements. *J. Comput. Phys.*, 63(2):416–433, 1986.

[50] D. L. Whitaker, B. Grossman, and R. Löhner. Two-Dimensional Euler Computations on a Triangular Mesh Using an Upwind, Finite-Volume Scheme. *AIAA-89-0365*, 1989.

[51] P. Woodward and P. Colella. The numerical simulation of two-dimensional fluid flow with strong shocks. *J. Comput. Phys.*, 54(1):115–173, 1984.